

Journal of Biomedical Optics

BiomedicalOptics.SPIEDigitalLibrary.org

Full anterior segment biometry with extended imaging range spectral domain optical coherence tomography at 1340 nm

Peng Li
Murray Johnstone
Ruikang K. Wang

Full anterior segment biometry with extended imaging range spectral domain optical coherence tomography at 1340 nm

Peng Li,^a Murray Johnstone,^b and Ruikang K. Wang^{a,b,*}

^aUniversity of Washington, Department of Bioengineering, Seattle, Washington 98195

^bUniversity of Washington, Department of Ophthalmology, Seattle, Washington 98104

Abstract. We demonstrate an extended-imaging-range anterior-segment optical coherence tomography (eAS-OCT) system for the biometric assessment of full AS in human eye. This newly developed eAS-OCT operating at 1340-nm wavelength band is simultaneously capable of an imaging speed of 120 kHz A-line scan rate, an axial resolution of 7.2 μm , and an extended imaging range of up to 16 mm in air. Imaging results from three healthy subjects and one subject with a narrow-angle demonstrate the instrument's utility. With this system, it can provide anatomical dimensions of AS, including central corneal thickness, anterior chamber width, anterior chamber depth, crystalline lens vault, crystalline lens thickness, angle opening distance (AOD500/AOD750), and the area described by the trabecular-iris space (TISA500/TISA750) at 500/750 μm . We also use eAS-OCT to image and quantify dynamic functional changes of the AS in response to a light stimulus that induces physiological pupillary changes as well as accommodative efforts that induce lens changes. The results show that the described eAS-OCT is able to provide full anatomical biometry for AS and is useful for the studies where the dynamic response of AS compartment to certain stimulus is required. © The Authors. Published by SPIE under a Creative Commons Attribution 3.0 Unported License. Distribution or reproduction of this work in whole or in part requires full attribution of the original publication, including its DOI. [DOI: 10.1117/1.JBO.19.4.046013]

Keywords: optical coherence tomography; full-range optical coherence tomography; biometry; anterior segment; ophthalmology.

Paper 140054R received Jan. 28, 2014; revised manuscript received Mar. 19, 2014; accepted for publication Mar. 24, 2014; published online Apr. 21, 2014.

1 Introduction

Optical coherence tomography (OCT) is now a popular high-resolution optical imaging technology¹ capable of providing images of internal microstructures within biological tissue. The most successful application of OCT has been in ophthalmology, where the technology has become an indispensable tool to image both the anterior segment (e.g., cornea and anterior chamber angle) and the posterior segment (e.g., retina) of the human eye. The OCT technology provides critical information aiding diagnosis, treatment, and management of a wide range of eye disorders. Izatt et al. were the first to report the use of OCT to noninvasively visualize the cornea and anterior chamber in 1994.² Since then, extensive efforts have been made to improve the technology and to explore the clinical utility of anterior-segment OCT (AS-OCT). Clinical uses include evaluating iridocorneal angle and identifying risk factors in primary angle closure glaucoma (PACG),^{3–13} visualizing cornea, anterior chamber, and crystalline lens in refractive surgery, such as in laser *in situ* keratomileusis (LASIK) and phakic or pseudophakic intraocular lens (IOL) implantation,^{14–20} assessing the dynamic response of AS during physiological accommodation and assessing ametropia, particularly for eyes undergoing IOL surgery.^{21–30}

While different applications have their own requirements for system performance, an ideal AS-OCT system for imaging AS should have (1) sufficient penetration depth so that anatomical features deep within corneoscleral limbus can be imaged; (2) $<10\text{-}\mu\text{m}$ axial resolution for visualizing sufficient anatomic

details; (3) $>10\text{-mm}$ image ranging distance; (4) sufficient imaging contrast for comprehensive evaluation of the whole anatomy from anterior cornea to posterior crystalline lens in one scan; and (5) $>100\text{-kHz}$ line-scan rate for rapid acquisition of the complete three-dimensional (3-D) OCT dataset of the whole segment within an acceptable time frame.

Currently, several commercial AS-OCT systems are available for clinical use (Table 1), which can be classified into time-domain (TD), swept-source (SS), and spectral-domain (SD) based configurations. Among them, both the TD-based and the SS-based AS-OCTs operate as a stand-alone system dedicated to AS imaging. The preference of operating wavelength band for these systems is $\sim 1310\text{ nm}$ because longer wavelength offers deeper penetration depth at the iridocorneal angle,^{31,32} permitting quantitative characterization of tissue spaces from the anterior cornea to the posterior crystalline lens.^{12,14,17,21}

Due to its inherent signal-to-noise ratio advantage, the Fourier-domain (FD) OCT (including SS-based and SD-based configurations) offers higher imaging speed (up to ~ 20 to 40 kHz line-scan rate) than those based on TD configuration. Even at these imaging speeds it remains challenging to avoid the motion artifacts and to acquire a high-quality 3-D OCT dataset of the whole AS within a clinically practical time frame. However, such a 3-D OCT imaging is a necessary requirement for comprehensive screening of cornea/anterior segment disorders. Furthermore, the current ranging distance (imaging depth) of ~ 6 to 7 mm precludes the imaging of full AS (from anterior cornea to posterior crystalline lens) in one scan, a capability highly beneficial for understanding anatomical/optical

*Address all correspondence to: Ruikang K. Wang, E-mail: wangrk@uw.edu

Table 1 Comparison of commercially available anterior-segment optical coherence tomography (AS-OCT) systems.

	Time-domain-based AS-OCT	Spectral-domain-based AS-OCT	Swept-source-based AS-OCT
Central wavelength	@ 1310 nm	@ 830 nm	@ 1310 nm
Axial resolution	>15 μm	<10 μm	~10 μm
Imaging depth range	~6 to 7 mm	~2 to 3 mm	~6 mm
Line-scan rate	2 kHz/200 Hz	~20 to 40 kHz	30 kHz
Commercialization	Zeiss Visante & Heidelberg SL-OCT	Currently the prevailing commercial OCT system ^a	Tomey CASIA
Function	Dedicated to AS imaging	Both retinal and AS imaging	Dedicated to AS imaging

^aOptovue RTVue, Optovue iVue, Zeiss Cirrus, Heidelberg Spectralis, Bioptigen Envisu, Optopol Copernicus.

conditions in AS. Such an understanding is essential for the management of the cornea in refractive surgery, the management of the anterior chamber angle in PACG,^{7-9,11-13,33} and the management of IOL decisions at cataract surgery as well as in evaluating the mechanisms of dynamic lens accommodation.²⁴⁻²⁸

To address the imaging speed limitation, several custom-built AS-OCTs with enhanced system performance have been developed. However, the complex conjugate artifact (inherent in FD-OCT) and the spectral-sampling density in the detecting spectrometer (available number of pixel array detectors in line-scan camera) represent limitations that impose constraints on the ranging distance of the SD-based AS-OCT systems. In the earlier AS-OCT systems, the usable ranging distance was doubled by resolving the complex conjugate artifact. The doubling enhances the ability to visualize anterior crystalline lens,^{34,35} delivering results comparable to those of the conventional TD-based AS-OCT systems.

Recently, a prototype ~830-nm band AS-OCT system was demonstrated that is based on 2048 and 4096 pixel line-scan cameras (increasing the spectral-sampling density of detectors).²⁸ By combining the higher pixel density with the full-range complex technique, an imaging depth of up to ~14 to 16 mm was achieved, thereby successfully covering the full AS.^{28,36} However, due to the higher light scattering at shorter wavelengths compared to the 1050/1300-nm systems, the 830-nm systems suffer from shallower penetration depths at the corneal limbus.^{31,32,37}

Benefiting from the rapid development of swept laser source technology, several SS-based AS-OCT systems have been demonstrated.^{25,38-41} Generally, due to the performance tradeoffs between imaging depth, imaging speed, and axial resolution, few of the SS-OCTs are able to provide concurrent features of high resolution (<10 μm), ultrafast speed (>100 kHz), and sufficient ranging distance (>12 mm) for 3-D imaging of the entire AS. Recently, a new swept laser based on a MEMS tunable vertical cavity surface-emitting laser (VCSEL) was demonstrated for SS-OCT imaging,⁴² offering negligible sensitivity roll-off over 1.0 cm depth. The swept laser system provides the balanced system performances among penetration depth (working at 1060-nm wavelength), axial resolution (9 μm), imaging depth (13.6 mm), and imaging speed (100 kHz line-scan rate), which are much more attractive for imaging the full AS.⁴²

In parallel to the development of SS-OCT, an extended-imaging-range SD-OCT (eSD-OCT) system⁴³ was proposed for AS imaging, delivering performance comparable to that of

a typical AS-OCT based on MEMS tunable VCSEL.⁴² Although the VCSEL-based AS-OCT system provided superior sensitivity roll-off performance,⁴² the eSD-OCT also successfully demonstrated the capability of full AS imaging in one scan with axial resolution and imaging speed similar to that of VCSEL-based ASOCT.⁴³ An advantage of the eSD-OCT system is its usage of the same types of technology as the 1050-nm band. Adoption of this standard technology then permits the use of almost all relatively inexpensive, readily available components in the current commercial systems. In particular, the eSD-OCT is based on the SD configuration. Compatibility with the current standard commercial SD-OCT systems provides an inherent advantage because it offers potential for a straightforward manufacturing and clinical translation.

In this study, we report a newly developed SD-based eAS-OCT operating at 1340 nm wavelength band that is capable of simultaneous 7.2 μm imaging resolution, 16 mm ranging distance, and 120 kHz A-scan rate. We then demonstrate static/anatomical full biometry of AS, investigating dynamic lens accommodation and studying the responses of AS compartments to light stimulation using the proposed eAS-OCT. Finally, we discuss the superiority, limitation, and potential applications of eAS-OCT for cornea, cataract, IOL, glaucoma, and refractive surgeries.

2 Material and Methods

The schematic of the prototype eAS-OCT used in this study is shown in Fig. 1, similar to the system reported in Ref. 43. A broadband superluminescence diode with a central wavelength of 1340 nm and a spectral bandwidth of 110 nm (LS2000B, Thorlabs Inc., USA) is used to illuminate the system, providing an axial resolution of ~7.2 μm in air. This light source gives an enhanced penetration for OCT imaging, facilitating the visualization of the iridocorneal angle due to reduced light scattering in tissue compared to light sources with shorter wavelengths. In addition, an objective lens with a 100 mm focal length is installed in the sample arm offering a lateral resolution of ~50 μm and a depth of focus of ~3 mm. The focal plane of the objective lens is placed at the zero-optical-length-difference plane, which is situated close to the iris for balanced imaging quality of full AS. The detection system is a high-speed spectrometer equipped with a transmission diffraction grating (Wasatch Photonics, USA) with 1145 lines/mm, an achromatic camera lens with a focal length of 100 mm, and a prototype InGaAs line-scan camera with a 2048 pixel-array detector

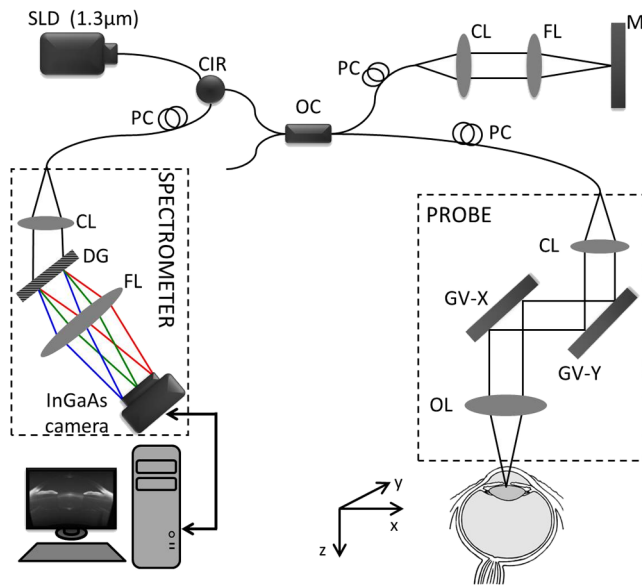


Fig. 1 Schematic of the spectral-domain-based extended imaging depth anterior-segment optical coherence tomography system setup. CIR, circulator; OC, optical coupler; CL, collimating lens; FL, focusing lens; M, mirror; GV, galvanometer; OL, objective lens; DG, diffraction grating; PC, polarization controller.

capable of a line-scan rate of 120 kHz (Sensors Unlimited Inc., part of United Technologies Aerospace Systems, USA). The spectral resolution of the spectrometer is 0.056 nm, offering a measured imaging range of ~ 8 mm and a sensitivity roll-off of 6 dB/4 mm. After removing the complex conjugate artifact using a full-range complex technique,^{44–46} the resultant imaging depth (ranging distance) is extended to ~ 16 mm in air. With this design, the system sensitivity at 0.5 mm depth is measured at ~ 100 dB.

In the sample arm, the scanner is designed to provide a telecentric scan in horizontal plane for minimal optical distortion.^{47,48} For imaging, two raster scanning patterns are designed to drive the X-Y scanner: static 3-D mode and dynamic two-dimensional (2-D) mode. In static 3-D mode, each B-frame is composed of 3000 A-lines with 2048 pixels per line, providing a high resolution and high definition cross-sectional image while fulfilling the requirement to achieve a full-range SD-OCT.^{28,43,46} With a 120-kHz line-scan rate, it takes ~ 2.5 s to complete a 3-D scan consisting of $2048 \times 3000 \times 100$ voxels ($16 \times 16 \times 12$ mm³ in air). For dynamic 2-D mode, the Y-scanner is disabled. The imaging is performed by repeated scanning at the same B-scan location. The duration of the scan is ~ 8.25 s, allowing a total of 330 successive cross-sectional images to be acquired for assessing dynamic activities of the human eye.

We then demonstrate the system's capability to provide anatomical biometry for full AS, to study dynamic behavior resulting from lens accommodation and to study effects caused by light stimulation. During imaging, the sample is exposed to a light power of 2.0 mW, within the American National Standards Institute safety limit. The use of in-house OCT systems to image the AS of the human eyes was approved by the institutional review board at the University of Washington. Before imaging, informed consent was obtained from each subject.

For biometric analyses of the AS, optical distortion in OCT images was corrected based on Snell's principle,⁴⁸ in which the

refractive indices of 1.38, 1.34, and 1.42 were used for cornea, aqueous humor, and crystalline lens, respectively.²⁵ The cross-sectional slice including the corneal vertex location was extracted from the 3-D dataset at the horizontal meridian by using a custom semiautomatic algorithm. The distal limit of each angle recess was identified and marked. The distance from recess to recess was recorded as the anterior chamber width (ACW). A recess-to-recess line was drawn, and its perpendicular projection extending from the median point passing through the anterior cornea and posterior crystalline lens was generated (refer to Fig. 2). The perpendicular line can be considered as the anteroposterior (AP) axis. Several quantitative parameters, defined along the AP axis, were measured in this study. Table 2 summarizes the definition of these parameters: the central corneal thickness (CCT), AC depth (ACD), the crystalline lens vault (LVa), and the crystalline lens thickness (LT). These parameters have been defined and measured respectively in previous studies.^{14,17,21,24,49}

To quantify iridocorneal angle configuration (refer to Fig. 3), the scleral spur was first marked. Based on this landmark, the perpendicular distances from the trabecular meshwork to the iris at 500 and 750 μ m anterior to scleral spur were automatically recorded as the angle opening distance (AOD500 and AOD750, respectively).^{3,6,50} The trabecular-iris space area at 500/750 μ m (TISA500 and TISA750, respectively) was also calculated as the trapezoidal area bounded anteriorly by the AOD500 or AOD750, posteriorly by a line perpendicular to the inner scleral wall at the scleral spur, superiorly by the inner corneoscleral wall, and inferiorly by the iris surface.^{3,5,6}

Additionally, the radius of crystalline lens anterior surface (LR) was determined by measurements that permitted circular fitting to the anterior lens surface. In the same manner, the radius of cornea anterior and posterior surface (CRA and CRp) can be quantified. Pupil diameter (PD) was calculated as pupil margin-to-margin distance.

2.1 System Performance Assessment

To assess how accurate the eAS-OCT system is to the biometric assessments of the key parameters, we elected to use a commercially available model eye (OEMI-7, Ocular Instruments Inc., Bellevue, WA) because its dimensions are known in prior. The model eye is composed of main ocular parts, including the cornea, pupil, crystalline lens, aqueous and vitreous media, as well as the retinal surface. The cornea and lens are composed of poly(methyl methacrylate) ($n = 1.49$), with the deionized water ($n = 1.33$) serving as the aqueous and vitreous media. 3-D OCT imaging was performed and repeated five times (the eye was repositioned into the system each time). The AS parameters of the model eye were measured. Because there is no angle recess in the model eye, the AP axis was determined based on the pupil for the system performance assessment.

2.2 Anatomical Biometry for Full Anterior Segment

Study enrollment to demonstrate the utility of eAS-OCT included four healthy subjects. Three of them (ages 23, 31, and 46) had no history of ocular disease and only modest refractive errors (0, -3 diopter, and -1 diopter, respectively). The fourth was a narrow-angle glaucoma suspect (age 24). Only the undilated right eye of each subject was imaged. The imaging was performed in a room with ~ 500 lux interior illumination.

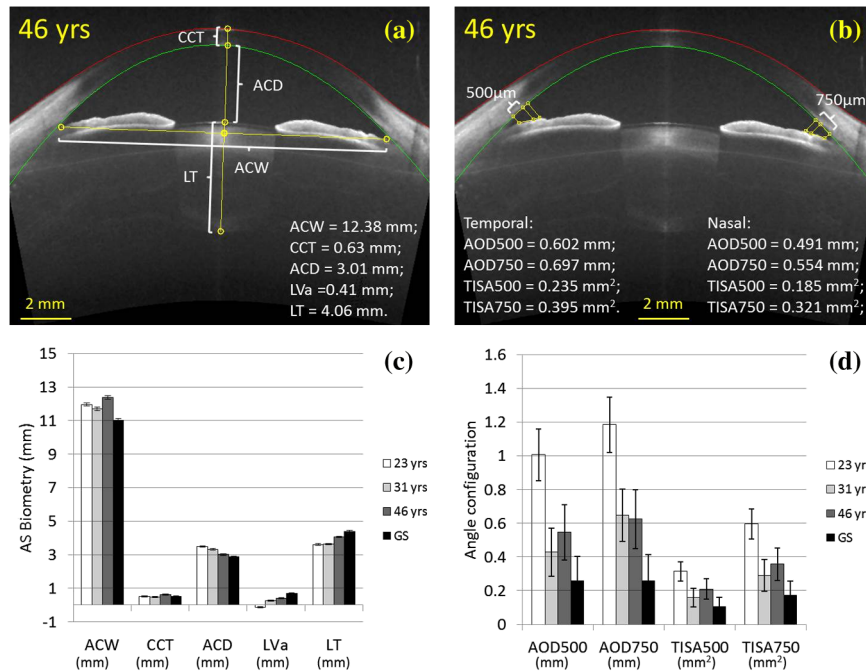


Fig. 2 Representative biometry illustrating the quantitative evaluation of (a) anatomic architectures and (b) iridocorneal angle configurations for a 46-year-old healthy subject in a relaxed state. (c) and (d) Quantitative measurements (mean ± std) of the anatomic architecture and iridocorneal angle configuration from each of the four subjects.

Each imaging session was repeated five times for each eye (repositioning was required from the subject each time). During scanning, subjects were instructed to fixate on a distant target consisting of an “E” to ensure an absence of accommodation. The AS parameters and iridocorneal angle configuration were determined for each eye.

2.3 Lens Accommodation

To demonstrate the capability of imaging the lens response to accommodation, we used the system to image a 31-year-old subject who first was instructed to fixate on a distant target “E” [0 D (diopter), accommodation relaxed]. The subject was then instructed to fixate on a second target “E” set at a distance

of 0.11 m, providing a 9 D accommodative stimulus. In addition to the parameters listed in Table 2, LR and PD were also calculated.

2.4 Light Stimulation

Dynamic 3-D imaging is challenging using the currently available AS-OCT imaging speeds. Therefore, to demonstrate the benefits of the eAS-OCT system, imaging was initially conducted under a bright (~500 lux) and a dark (<1 lux) background, respectively. Room illumination was then dimmed to <1 lux. As illustrated in Fig. 4, the subject was asked to fixate on a laboratory-designed light-emitting diode target flashing at a frequency of ~1 Hz; the scanning protocol was then switched to the dynamic 2-D mode to capture the real-time dynamic response to the flashing light stimulus.

Table 2 Definition of AS parameters.

AS parameters	Distance from A to B	
	A	B
Anterior chamber width	Recess	Recess
CCT ^a	Corneal surface	Corneal endothelium
ACD ^a	Corneal endothelium	Anterior crystalline lens surface
LVa ^a	Anterior crystalline lens surface	Recess-to-recess line
LT ^a	Anterior crystalline lens surface	Posterior crystalline lens surface

CCT, central corneal thickness; ACD, anterior chamber depth; LVa, crystalline lens vault; LT, crystalline lens thickness.

^aDistance along anteroposterior axis.

3 Results

3.1 System Performance Assessment

Figure 5 shows a typical cross-sectional eAS-OCT image captured from the model eye, where the boundaries of cornea and lens can be visualized. The biometric assessment of this model eye is tabulated in Table 3, along with the values provided by the manufacturer. These data indicate that the eAS-OCT can deliver the biometric measurements with very good accuracy. In addition, the system also provides good consistency between each imaging session (as demonstrated by the small values of standard deviation).

3.2 Biometry of the Full Anterior Segment

Figure 6 shows the horizontal cross-sections acquired from the four subjects, each in a state of relaxed accommodation.

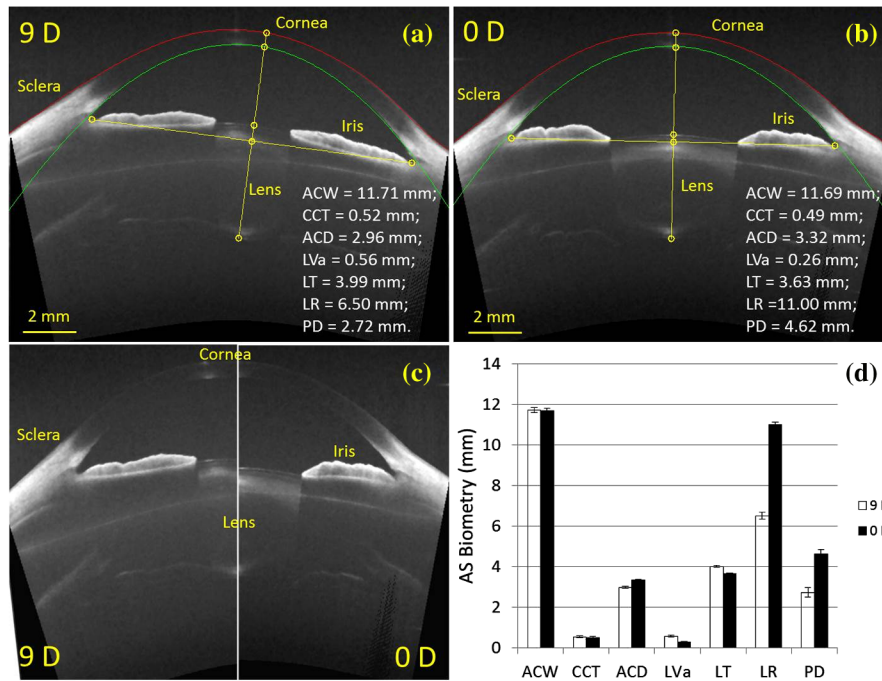


Fig. 3 Horizontal cross-section of the anterior segment of a 31-year-old healthy subject (a) in the accommodated state (9 D accommodative stimulus) and (b) in the relaxed state (no accommodation). (c) Composite image of (a) and (b) after aligning the corneas along the plane of the anteroposterior axis of each image. (d) Chart indicates the changes in the architecture of anterior segment in response to accommodation (values given = mean \pm std).

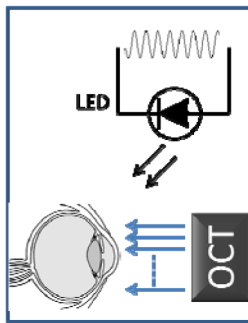


Fig. 4 Schematic of the light stimulus module.

The primary anatomic features in AS are clearly visible in the eAS-OCT images, including cornea, sclera, iris, and crystalline lens. More importantly, important landmarks necessary for the biometric assessment of AS can be easily identified, such as the scleral spur and angle recess (arrows in Fig. 6). Using these landmarks, the quantitative evaluation of the full anatomic architecture and iridocorneal angle configuration are readily achieved, as illustrated in Figs. 2(a) and 2(b), respectively.

Based on the biometric assessments for healthy subjects, the mean values of the parameters are $CCT = 0.56 \pm 0.06$ mm, $ACW = 12 \pm 0.57$ mm, $ACD = 3.25 \pm 0.28$ mm, $LVa = 0.26 \pm 0.34$ mm, and $LT = 3.77 \pm 0.36$ mm. These derived values are in good agreement with previously reported ones by other groups using different AS-OCTs, including custom-built and commercial TD-based AS-OCTs,^{12,14,17,21,29,51} SS-based AS-OCT,^{25,49} and SD-based AS-OCT.²⁶ Furthermore, our results for ACD, LVa, and LT are in agreement with age-related correlations reported in previous publications.^{12,13,21,23}

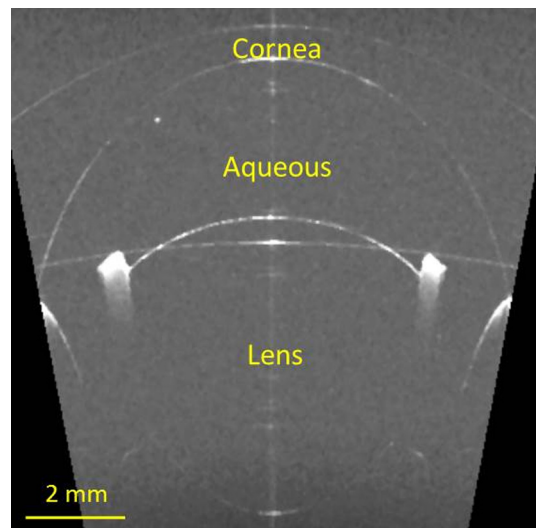


Fig. 5 Cross-section of model eye.

Table 3 Results assessed from the model eye.

	CCT	ACD	LT
Manufacturer values \pm tolerance (mm)	0.55 ± 0.13	2.95 ± 0.51	3.9 ± 0.51
OCT values \pm std (mm)	0.49 ± 0.01	3.03 ± 0.01	3.86 ± 0.01

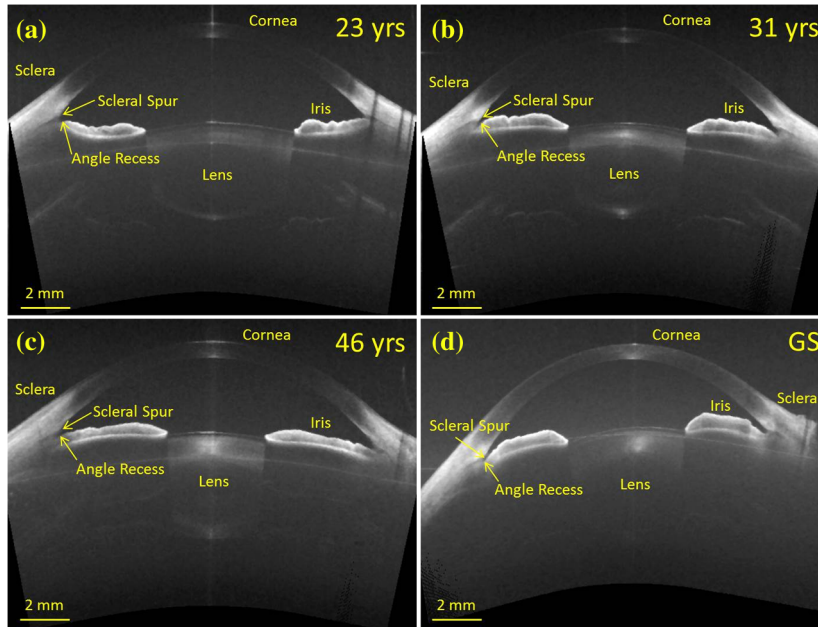


Fig. 6 Horizontal cross-sections of anterior segment, under conditions of relaxed accommodation, acquired from three healthy subjects aged (a) 23, (b) 31, (c) 46, and (d) an angle-closure glaucoma suspect age 24.

The parameters for iridocorneal angle configuration, e.g., AOD500 (mean = 0.66 mm), AOD750 (mean = 0.82 mm), TISA500 (mean=0.23mm²), and TISA750 (mean=0.42mm²), are within the same range as the measurements reported in Refs. 3, 5, and 6. The small variances seen in our study compared with previous reports are most likely due to individual iris and lens factors.^{12,13} The youngest subject has the most concave

iris, largest pupil size, and weakest OCT signal in the crystalline lens while having the widest iridocorneal angle, consistent with expected findings for young subjects.

By contrast, for the narrow angle suspect, we observe not only narrower angle configuration, but also smaller ACD, larger LVA and LT, obvious iris convexity, and increased thickness of the iris compared to those observed from subjects who were not

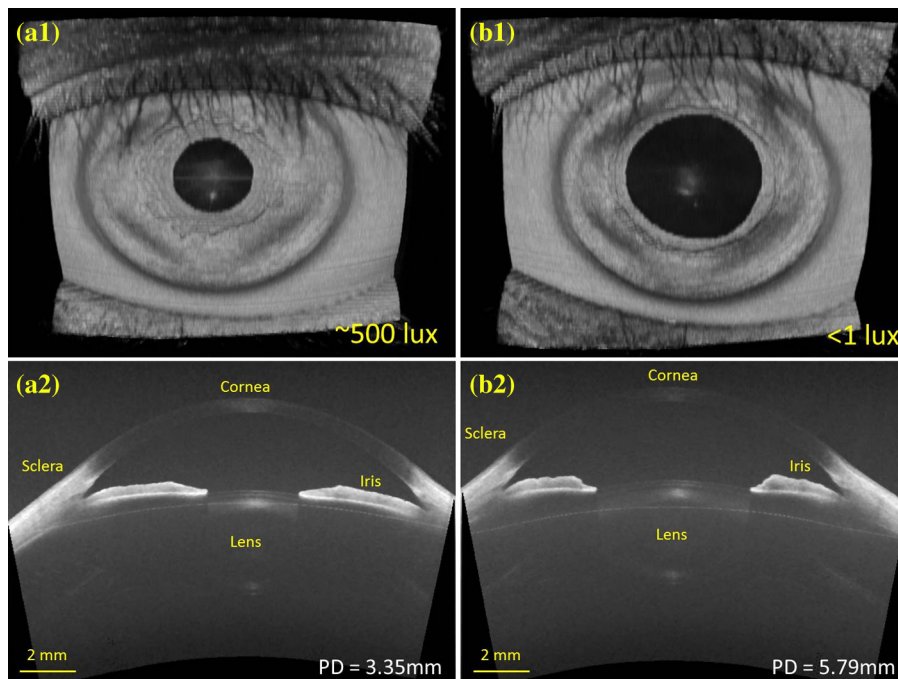


Fig. 7 Extended-imaging-range anterior-segment optical coherence tomography (AS-OCT) images of a 31-year-old healthy subject under (a) bright (~500 lux) and (b) dark (<1 lux) room illumination, respectively. The first row [(a1) and (b1)] shows the en-face view of the three-dimensional volume. The second row [(a2) and (b2)] shows the corresponding representative cross-sections (PD is pupil diameter).

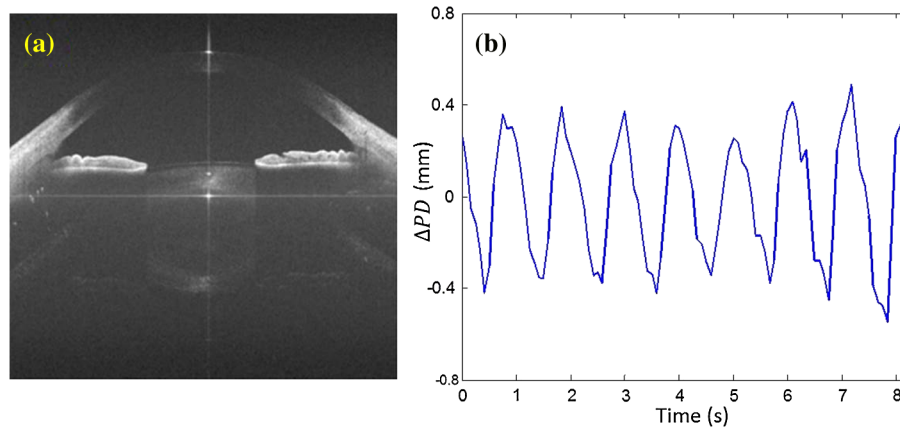


Fig. 8 Dynamic pupillary reaction of the eye of a 31-year-old healthy subject subjected to a series of flashing light stimuli. (a) Typical OCT cross-sectional image of the AS of the subject during light stimulation (Video 1, MOV, 2.57 MB) [URL: <http://dx.doi.org/10.1117/1.JBO.19.4.046013.1>]. (b) The corresponding flashing-light-dependent change of pupil diameter (PD).

angle closure suspects. All of these findings are in excellent agreement with recent studies on PACG that reported a significant relationship of angle closure to anterior chamber, iris, and lens parameters, such as ACD, iris thickness, iris curvature, LVa, and LT.^{7-9,11-13,33,52}

3.3 Lens Accommodation

Figure 3 summarizes accommodation-dependent geometric responses of the AS determined by eAS-OCT. Obvious changes can be found in ACD (-0.36 mm decrease), LVa ($+0.30$ mm), LT ($+0.36$ mm thickening), LR (-3.5 mm), and PD (-1.9 mm) after inducing 9 D of accommodation; at the same time, negligible changes are observed in ACW and CC.

The measured geometrical changes of the AS during accommodation indicate that several actions occur in response to an accommodative effort: (1) the lens thickness is increased; (2) the anterior lens pole moves toward the cornea, while the posterior pole changes only to a small extent; (3) the anterior lens surface becomes convex (most likely due to the decrease of the lens diameter); (4) synkinetic myosis occurs; and (5) the iris becomes concave due to the upward movement of anterior pole of the lens. All these observations are in accordance with the accommodation theory described in Ref. 53. However, the mechanism of accommodation is still not completely understood. The capability of visualizing and quantitatively assessing the *in vivo* 3-D architecture of the AS in a noncontact and non-invasive fashion provides a powerful, user-friendly approach to gain further understanding of the mechanism of accommodation and the changes associated with ametopia and aging.

3.4 Light Stimulation

Figure 7 shows the results from the eAS-OCT imaging under bright (~ 500 lux) and dark (< 1 lux) room illumination, respectively. The iris thickness is increased and the pupil is dilated considerably under dark illumination (2.44 mm increase in pupil diameter) compared to that under bright room illumination. Figure 8 shows the real-time dynamic cross-sectional imaging of the same subject in response to a flashing light stimulus. The PD undergoes oscillatory change in size that is synchronous with the flashing light as plotted in Fig. 8(b).

4 Discussion and Conclusions

PACG is one of the leading causes of blindness, especially prevalent in Asian population, and is characterized by closure of the iridocorneal angle. Recent studies indicate that several important factors may be associated with the angle closure, such as ACD, LVa, LT, iris thickness, iris curvature, and iris dynamics.^{7-13,33,52,54,55} We have demonstrated that eAS-OCT is capable of evaluating the angle configuration and providing quantitative assessments of all these parameters using one device. Therefore, we believe that eAS-OCT may become an efficient imaging tool for better understanding of the risk factors and pathogenesis in angle closure. By quantitatively assessing the parameters that increase PACG risk, patients can be better identified and decisions about monitoring or intervention can be made based on the combination of objectively obtained parameters.

In recent years, refractive surgeries, including corneal laser ablation surgery and phakic or pseudophakic IOL implantation, have been increasingly used for the refractive correction of patient eyes, but planning of such surgeries present several challenges.^{15,16,56-58} To provide optimal postoperative refractive results, precise preoperative measurements of anatomical dimensions (CCT, ACD, ACW, LVa, and LT) in AS are essential. The eAS-OCT is able to accurately quantify not only the anatomic dimensions of the full AS, but also the anatomic changes that characterize the functional parameters associated with accommodation. This extended performance has clear implication for clinical applications, including preoperative design/selection of appropriate surgery parameters, intraoperative surgery guidance, and postoperative evaluation, e.g., long-term assessment of procedure safety. In addition, this system provides a means for improving IOL designs through its ability to assess accommodation-induced IOL anterior-posterior position changes, while at the same time being able to characterize any associated design-dependent deformation of the IOL itself.

The proposed eAS-OCT is inherently compatible with the current standard commercial SD-OCT systems offering significant opportunities for consolidation of instrument functions. Integration of the SD-based eAS-OCT into commercial systems offers a combination of high resolution and fast speed of current SD-based AS-OCT, while at the same time providing the long ranging distance similar to that of the TD-based AS-OCT. With

simultaneous high axial resolution, fast imaging speed, and extended imaging depth consolidated into one device, the eAS-OCT may, in addition, find valuable applications in areas such as in the assessment of the health of ocular surfaces to determine effects and complications from medications used in open-angle glaucoma, assessment of positioning and behavior of intrastromal corneal rings, as well as decision guidance before and monitoring after corneal transplantation.

Nevertheless, the eAS-OCT described here still has several limitations. For example, the sensitivity roll-off is limited to ~ 6 dB/4 mm. With this limitation, however, sufficient signal has been obtained at the center of cornea and crystalline lens, which would make the system clinically acceptable for imaging the full AS. In addition, with a lateral resolution of $50 \mu\text{m}$, the current system offers a depth of focus of only ~ 3 mm, giving rise to reduced OCT signal strength for the tissue structures outside of the depth-of-focus region, creating a potential problem for imaging whole cornea that is typically of curved structure with increased oblique angle at the peripheral edge regions. This was the primary reason why the OCT signals were much weak at the oblique parts of cornea and crystalline lens in this study. In future, more sophisticated scanning optics needs to be designed, through synergistic optimization between the lateral resolution and the depth of focus.

In summary, we have designed and demonstrated clinically useful applications for a 1340-nm eAS-OCT that is capable of imaging the full AS at 120 kHz line-scan rate, at the same time attaining 16 mm imaging range and $\sim 7.0 \mu\text{m}$ axial resolution. Such an extended system performance permits visualization and quantification of the static/anatomical dimensions of the AS (i.e., biometry of the full AS). At the same time, this same device can characterize and quantitate several dynamic/physiological ocular parameters, such as the lens or IOL response to accommodative efforts and the pupil response to a light stimulus. Potential clinical applications could be found in cornea, cataract, IOL, glaucoma, and refractive surgeries.

Acknowledgments

The authors would like to thank Dr. Doug Malchow from United Technologies Aerospace Systems, USA, who generously provided the prototype InGaAs camera used in this project. This work was supported in part by research grants from the National Eye Institute (R01EY024158-01), the W.H. Coulter Foundation Translational Research Partnership Program, and unrestricted funds from Research to Prevent Blindness, Inc. Dr. Wang is a recipient of Research to Prevent Blindness Innovative Ophthalmic Research Award. The funding entities had no role in study design, data collection and analysis, decision to publish, or preparation of the manuscript.

References

- D. Huang et al., "Optical coherence tomography," *Science* **254**(5034), 1178–1181 (1991).
- J. A. Izatt et al., "Micrometer-scale resolution imaging of the anterior eye in vivo with optical coherence tomography," *Arch. Ophthalmol.* **112**(12), 1584–1589 (1994).
- S. Radhakrishnan et al., "Reproducibility of anterior chamber angle measurements obtained with anterior segment optical coherence tomography," *Invest. Ophthalmol. Vis. Sci.* **48**(8), 3683–3688 (2007).
- W. P. Nolan et al., "Detection of primary angle closure using anterior segment optical coherence tomography in Asian eyes," *Ophthalmology* **114**(1), 33–39 (2007).
- S. Radhakrishnan et al., "Comparison of optical coherence tomography and ultrasound biomicroscopy for detection of narrow anterior chamber angles," *Arch. Ophthalmol.* **123**(8), 1053–1059 (2005).
- C. K. Leung et al., "Anterior chamber angle measurement with anterior segment optical coherence tomography: a comparison between slit lamp OCT and Visante OCT," *Invest. Ophthalmol. Vis. Sci.* **49**(8), 3469–3474 (2008).
- S. Salim, "The role of anterior segment optical coherence tomography in glaucoma," *J. Ophthalmol.* **2012**, 476801 (2012).
- M. E. Nongpiur, J. Y. Ku, and T. Aung, "Angle closure glaucoma: a mechanistic review," *Curr. Opin. Ophthalmol.* **22**(2), 96–101 (2011).
- B. Wang et al., "Quantitative iris parameters and association with narrow angles," *Ophthalmology* **117**(1), 11–17 (2010).
- C. Zheng et al., "Analysis of anterior segment dynamics using anterior segment optical coherence tomography before and after laser peripheral iridotomy," *JAMA Ophthalmol.* **131**(1), 44–49 (2013).
- N. Shabana et al., "Quantitative evaluation of anterior chamber parameters using anterior segment optical coherence tomography in primary angle closure mechanisms," *Clin. Experiment. Ophthalmol.* **40**(8), 792–801 (2012).
- J. H. Sun et al., "Factors associated with anterior chamber narrowing with age: an optical coherence tomography study," *Invest. Ophthalmol. Vis. Sci.* **53**(6), 2607–2610 (2012).
- M. E. Nongpiur et al., "Lens vault, thickness, and position in Chinese subjects with angle closure," *Ophthalmology* **118**(3), 474–479 (2011).
- J. A. Goldsmith et al., "Anterior chamber width measurement by high-speed optical coherence tomography," *Ophthalmology* **112**(2), 238–244 (2005).
- Y. Li et al., "A longitudinal study of LASIK flap and stromal thickness with high-speed optical coherence tomography," *Ophthalmology* **114**(6), 1124–1132 (2007).
- Y. Li, R. Shekhar, and D. Huang, "Corneal pachymetry mapping with high-speed optical coherence tomography," *Ophthalmology* **113**(5), 792–799 (2006).
- G. Baikoff, H. J. Jodai, and G. Bourgeon, "Measurement of the internal diameter and depth of the anterior chamber: IOLMaster versus anterior chamber optical coherence tomographer," *J. Cataract Refract. Surg.* **31**(9), 1722–1728 (2005).
- M. Doors et al., "Value of preoperative phakic intraocular lens simulation using optical coherence tomography," *J. Cataract Refract. Surg.* **35**(3), 438–443 (2009).
- M. Bechmann et al., "Imaging of posterior chamber phakic intraocular lens by optical coherence tomography," *J. Cataract Refract. Surg.* **28**(2), 360–363 (2002).
- G. Baikoff et al., "Contact between 3 phakic intraocular lens models and the crystalline lens: an anterior chamber optical coherence tomography study," *J. Cataract Refract. Surg.* **30**(9), 2007–2012 (2004).
- G. Baikoff et al., "Static and dynamic analysis of the anterior segment with optical coherence tomography," *J. Cataract Refract. Surg.* **30**(9), 1843–1850 (2004).
- G. Baikoff et al., "Anterior chamber optical coherence tomography study of human natural accommodation in a 19-year-old albino," *J. Cataract Refract. Surg.* **30**(3), 696–701 (2004).
- K. Richdale, M. A. Bullimore, and K. Zadnik, "Lens thickness with age and accommodation by optical coherence tomography," *Ophthalmic Physiol. Opt.* **28**(5), 441–447 (2008).
- C. Du et al., "Anterior segment biometry during accommodation imaged with ultralong scan depth optical coherence tomography," *Ophthalmology* **119**(12), 2479–2485 (2012).
- H. Furukawa et al., "Full-range imaging of eye accommodation by high-speed long-depth range optical frequency domain imaging," *Biomed. Opt. Express* **1**(5), 1491–1501 (2010).
- M. Ruggeri et al., "Imaging and full-length biometry of the eye during accommodation using spectral domain OCT with an optical switch," *Biomed. Opt. Express* **3**(7), 1506–1520 (2012).
- G. Shi et al., "Measurement of ocular anterior segment dimension and wavefront aberration simultaneously during accommodation," *J. Biomed. Opt.* **17**(12), 120501 (2012).
- I. Grulkowski et al., "Anterior segment imaging with spectral OCT system using a high-speed CMOS camera," *Opt. Express* **17**(6), 4842–4858 (2009).

29. P. S. Yan et al., "Anterior segment variations with age and accommodation demonstrated by slit-lamp-adapted optical coherence tomography," *Ophthalmology* **117**(12), 2301–2307 (2010).
30. J. L. Guell et al., "Evaluation of Verisyse and Artiflex phakic intraocular lenses during accommodation using Visante optical coherence tomography," *J. Cataract Refract. Surg.* **33**(8), 1398–1404 (2007).
31. S. A. Perera et al., "Imaging of the iridocorneal angle with the RTVue spectral domain optical coherence tomography," *Invest. Ophthalmol. Vis. Sci.* **53**(4), 1710–1713 (2012).
32. S. Radhakrishnan et al., "Real-time optical coherence tomography of the anterior segment at 1310 nm," *Arch. Ophthalmol.* **119**(8), 1179–1185 (2001).
33. G. Marchini et al., "Ultrasound biomicroscopic and conventional ultrasonographic study of ocular dimensions in primary angle-closure glaucoma," *Ophthalmology* **105**(11), 2091–2098 (1998).
34. M. V. Sarunic, S. Asrani, and J. A. Izatt, "Imaging the ocular anterior segment with real-time, full-range Fourier-domain optical coherence tomography," *Arch. Ophthalmol.* **126**(4), 537–542 (2008).
35. S. Asrani et al., "Detailed visualization of the anterior segment using Fourier-domain optical coherence tomography," *Arch. Ophthalmol.* **126**(6), 765–771 (2008).
36. J. Jungwirth et al., "Extended in vivo anterior eye-segment imaging with full-range complex spectral domain optical coherence tomography," *J. Biomed. Opt.* **14**(5), 050501 (2009).
37. P. A. Keane, H. Ruiz-Garcia, and S. R. Sadda, "Clinical applications of long-wavelength (1,000-nm) optical coherence tomography," *Ophthalmic Surg. Lasers Imaging* **42**(4), S67–74 (2011).
38. M. Gora et al., "Ultra high-speed swept source OCT imaging of the anterior segment of human eye at 200 kHz with adjustable imaging range," *Opt. Express* **17**(17), 14880–14894 (2009).
39. B. Potsaid et al., "Ultrahigh speed 1050 nm swept source/Fourier domain OCT retinal and anterior segment imaging at 100,000 to 400,000 axial scans per second," *Opt. Express* **18**(19), 20029–20048 (2010).
40. W. Wieser et al., "Extended coherence length megahertz FDML and its application for anterior segment imaging," *Biomed. Opt. Express* **3**(10), 2647–2657 (2012).
41. A.-H. Dhalla et al., "Simultaneous swept source optical coherence tomography of the anterior segment and retina using coherence revival," *Opt. Lett.* **37**(11), 1883–1885 (2012).
42. I. Grulkowski et al., "Retinal, anterior segment and full eye imaging using ultrahigh speed swept source OCT with vertical-cavity surface emitting lasers," *Biomed. Opt. Express* **3**(11), 2733–2751 (2012).
43. P. Li et al., "Extended imaging depth to 12 mm for 1050-nm spectral domain optical coherence tomography for imaging the whole anterior segment of the human eye at 120-kHz A-scan rate," *J. Biomed. Opt.* **18**(1), 016012 (2013).
44. R. K. Wang, "In vivo full range complex Fourier domain optical coherence tomography," *Appl. Phys. Lett.* **90**(5), 054103 (2007).
45. R. K. Wang, "Fourier domain optical coherence tomography achieves full range complex imaging in vivo by introducing a carrier frequency during scanning," *Phys. Med. Biol.* **52**(19), 5897–5907 (2007).
46. L. An and R. K. Wang, "Use of a scanner to modulate spatial interferograms for in vivo full-range Fourier-domain optical coherence tomography," *Opt. Lett.* **32**(23), 3423–3425 (2007).
47. V. Westphal et al., "Correction of geometric and refractive image distortions in optical coherence tomography applying Fermat's principle," *Opt. Express* **10**(9), 397–404 (2002).
48. M. Zhao, A. N. Kuo, and J. A. Izatt, "3D refraction correction and extraction of clinical parameters from spectral domain optical coherence tomography of the cornea," *Opt. Express* **18**(9), 8923–8936 (2010).
49. S. Fukuda et al., "Anterior ocular biometry using 3-dimensional optical coherence tomography," *Ophthalmology* **116**(5), 882–889 (2009).
50. C. J. Pavlin, K. Harasiewicz, and F. S. Foster, "Ultrasound biomicroscopy of anterior segment structures in normal and glaucomatous eyes," *Am. J. Ophthalmol.* **113**(4), 381–389 (1992).
51. Y. Zeng et al., "Comparison of lens thickness measurements using the anterior segment optical coherence tomography and A-scan ultrasonography," *Invest. Ophthalmol. Vis. Sci.* **50**(1), 290–294 (2008).
52. S. D. Potash et al., "Ultrasound biomicroscopy in pigment dispersion syndrome," *Ophthalmology* **101**(2), 332–339 (1994).
53. D.-E. Stewart and A. David, *System of Ophthalmology Vol 5: Ophthalmic Optics and Refraction*, The C V Mosby Company, St. Louis (1970).
54. H. A. Quigley et al., "Iris cross-sectional area decreases with pupil dilation and its dynamic behavior is a risk factor in angle closure," *J. Glaucoma* **18**(3), 173–179 (2009).
55. C. Zheng et al., "In vivo analysis of vectors involved in pupil constriction in Chinese subjects with angle closure," *Invest. Ophthalmol. Vis. Sci.* **53**(11), 6756–6762 (2012).
56. L. Espandar, J. J. Meyer, and M. Moshirfar, "Phakic intraocular lenses," *Curr. Opin. Ophthalmol.* **19**(4), 349–356 (2008).
57. M. Doors et al., "Value of optical coherence tomography for anterior segment surgery," *J. Cataract Refract. Surg.* **36**(7), 1213–1229 (2010).
58. S. Ortiz et al., "Full OCT anterior segment biometry: an application in cataract surgery," *Biomed. Opt. Express* **4**(3), 387–396 (2013).

Biographies of the authors are not available.